Supporting information

A Li^+-flux-homogenizing separator for long-cycle Li metal anodes

Yuanpeng Ji[1,2], Liwei Dong[1], Jipeng Liu[1], Haodong Xie[2], Shijie Zhong[2], Chunhui Yang[1,3], Jiecai Han[2], Weidong He[2,4,5]★

[1]MIIT Key Laboratory of Critical Materials Technology for New Energy Conversion and Storage, School of Chemistry and Chemical Engineering, Harbin Institute of Technology, Harbin 150080, China.

[2]National Key Laboratory of Science and Technology on Advanced Composites in Special Environments, and Center for Composite Materials and Structures, Harbin Institute of Technology, Harbin 150080, China.

[3]State Key Laboratory of Urban Water Resource and Environment, Harbin Institute of Technology, Harbin 150080, China.

[4]Chongqing Research Institute, Harbin Institute of Technology, Chongqing 401151, China.

[5]School of Mechanical Engineering, Chengdu University, Chengdu 610106, China.

E-mail: *weidong.he@hit.edu.cn*

Experimental section

Materials. The poly (vinylidene fluoride-co-hexafluoropropylene) (PVDF-HFP, Mw ~ 600,000 g mol^{-1}) powder and polyvinylidene fluoride (PVDF, Mw ~ 900,000 g mol^{-1}) powder are all purchased from Solvay Co., Ltd. (China). The super P, aluminum (Al) foil, polypropylene (PP) separator (Celgard 2500), and commercial electrolyte based on lithium hexafluorophosphate ($LiPF_6$) dissolved in the mixture of ethylene carbonate, dimethyl carbonate, diethyl carbonate, and ethyl methyl carbonate (30:15:20:35 by weight with 2% vinylene carbonate) are purchased from Guangdong Canrd New Energy Technology Co., Ltd. (China). Acetone and *N*-methyl-2-pyrrolidone (NMP) are purchased from Aladdin (China). $LiFePO_4$ (LFP) is provided by Dongfang Electric Corporation (China). Li metal foils are obtained from China Energy Lithium Co., Ltd. (China). Antistatic agent SN (Octadecyl dimethyl hydroxyethyl quaternary ammonium nitrate) aqueous solution is purchased from Shanghai Makclin Biochemical Co., Ltd. (China).

Preparation of separators. 0.7g PVDF-HFP powders and 10 wt.% antistatic agent SN (compared to the weight of PVDF-HFP) are dissolved in 7 mL acetone, followed by stirring at 60 °C for 1 h. After cooling down to room temperature, the uniform mixture of antistatic agent SN (SN) and PVDF-HFP is coated on a flat steel substrate using a doctor blade to produce a separator with uniform thickness. The composite separator is marked as PVDF-HFP/SN. As for the preparation of the pure PVDF-HFP separator, 0.7g PVDF-HFP powders are added into 7 mL acetone stirring at 60 °C for half an hour, and then the same amount of deionized water compared to the antistatic

agent SN solvent is dropped into the solution stirring at 60 °C for another half. The remaining steps are similar to the preparation of the PVDF-HFP/SN separator.

Preparation of $LiFeO_4$ cathode. $LiFePO_4$ powder, super P, and PVDF with the ratio of 8:1:1 is dispersed into NMP solvent stirring for 12 h at room temperature to form a uniform slurry. After the slurry is cast on an Al foil and dried at 80 °C for 12 h in a vacuum oven, the cathode is cropped into circular discs with d = 12 mm used for battery assembly. And the average mass of $LiFePO_4$ is 2.8 ± 0.2 mg cm^{-2}.

Material characterization. The morphology of the pure PVDF-HFP separator and PVDF-HFP/SN separators and elemental analyses mapping are characterized using field emission scanning electron microscope (FE-SEM, ZEISS SUPRA 55, Carl Zeiss, Germany). The pore size distribution of different separators is measured by capillary flow porometer (BSD-PB, Beishide, China). X-ray diffraction (XRD, D8 AdvanceX, Bruker, Germany) is performed to measure the crystalline structure of the separators with Cu Kα radiation source over the 2θ range of 10° - 60°. Fourier transform infrared spectra (FT-IR) are tested by Nicolet iS5 (Thermo Fisher Scientific, USA). Raman spectra are taken with inVia-Reflex (Renishaw, England). The porosities of different separators are measured via mercury porosimetry (Autopore V9620, Micromeritics Instrument, USA). X-ray photoelectron spectroscopy (XPS) is carried out to analyze the elemental information on the surface of PVDF-HFP/SN separators and cycled Li metal anode using the Thermo Scientific K-Alpha+ (Thermo Fisher Scientific, USA). Time-of-flight secondary ion mass spectroscopy (TOF-SIMS, TOF.SIMS 5, ION-TOF, Germany) is conducted to value the ion fragments on the cycled Li metal anodes.

Gurley number of the separator is conductd via air permeability tester (RH-TQ100, China). Tensile strengths of the separators are attained using a tensile testing machine (CMT6104, China) at a tensile speed of 50 mm min^{-1} and the width of the sample is 20 mm. The surface contact angle between the electrolyte and separator is measured by ThetaLite (Biolin instrument, Finland) to evaluate the wettability of the separators. The sample preparation process for testing the ion concentration in the electrolyte is described as follows: 20 round pieces of PVDF-HFP/SN separators, with a diameter of 16 mm, are immersed in 1 mL electrolyte, consistent with the 50 μL dosage used in the cell assembly process. After immersion for one week, both the modified electrolyte and the bare electrolyte are diluted 500 times. Subsequently, the ion concentrations of Li^+ and NO_3^- in the electrolytes are analyzed using ion chromatography (IC, Thermo Fisher Scientific, USA).

Electrochemical measurements. All electrochemical tests are carried out at room temperature using CR2025 coin cells containing 50 μL electrolyte, which is assembled in the glove box (argon atmosphere environment, <0.1 ppm of H_2O and <0.1 ppm of O_2). The ionic conductivity of the separator is evaluated by electrochemical impedance spectroscopy (EIS) using a CHI760e (Shanghai Chenhua, China) electrochemical workstation at a frequency range of 1×10^6 to 1 Hz and the amplitude voltage is 5 mV. A stainless-steel (SS) symmetric cell is used in the ionic conductivity test and the ionic conductivity is computed using the equation below:

$$\sigma = \frac{l}{RA} \quad (1)$$

where l and A refer to the thickness (cm) and the effective contact area (cm^2) of the

separators. R (Ohm, Ω) represents the bulk resistance of the separator evaluated with the EIS test. The diameter of the SS electrode in this calculation is 1.56 cm and the area of the SS electrode is regarded as the contact area in the SS||SS cell. The lithium-ion transference number (t_{Li^+}) of the separator is determined by the steady-state current method measuring the impedance and DC polarization of Li symmetric cells. The t_{Li^+} is calculated using the following equation:

$$t_{Li+} = \frac{I_S(\Delta V - I_0 R_0)}{I_0(\Delta V - I_S R_S)} \quad (2)$$

where the R_0 and R_S are the initial and steady-state resistances, as obtained through the impedance measurements before and after the chronoamperometry measurement. ΔV, I_0 and I_S stands for the constant voltage step value (10 mV), initial current, and steady-state current from the chronoamperometry measurement, respectively. Li||Li symmetric cells are tested under a constant current of 0.5 mA cm^{-2} for 2 h. Full cells of Li metal batteries fabricated with LFP cathode (1C = 170 mA h g^{-1}) are utilized to evaluate the rate and cyclic performance of the separator through a battery testing system (NEWARE, China) in the voltage window of 2.5 V - 4.2 V. Cyclic Voltammetry (CV) is conducted in the voltage range of 2.5 V - 4.2 V at a scan rate of 0.1 mV s^{-1}. EIS is performed in the condition of 1.0 MHz - 0.1 Hz with 5 mV oscillating voltage at the open current potential of the battery. The Tafel plots are obtained from the built-in TAFEL method in the electrochemical workstation (CHI760E) using symmetric cells. The dendrites' growth is observed via an *in-situ* optical microscopy with a high-definition digital electronic camera and a special electrochemical cell with glass window (Tianjin Aida Hengsheng, China). The tests are performed at a current density

of 10 mA cm^{-2}.

Density functional theory calculation. The electrostatic potential of the $(VDF)_3$-$(HFP)_3$ molecule and the Mulliken charge population of the SN molecule are calculated by the density functional theory (DFT) implemented with the Dmol[3] package. B3LYP in conjunction with the basis set of DNP is performed during the calculation. The charge density difference and the binding energy of SN-NO_3 and SN-PF_6 are performed using the Vienna Ab initio Simulation Package. The binding energy is calculated with the equation: $E = E_{a-b} - (E_a + E_b)$, where E is the binding energy, and E_{a-b} is the total energy of the relaxed a and b models at the equilibrium state. Perdew-Burke-Ernzerhof (PBE) exchange-correlation functional within the generalized gradient approximation (GGA) is used to describe the exchange-correlation energy. The plane-wave expansion is cut off at 450 eV. Because of the large size of the cells, only the Gamma point in the reciprocal space is used in our calculation. Note that the PVDF-HFP used in the charge density difference plots is modeled from the α-PVDF by changing one VDF to HPF every three units because no crystal structure of PVDF-HFP is available in the crystallographic database[1, 2], and this PVDF-HFP is optimized before calculation. Calculations are performed under an implicit solvation model with dielectric properties of EC (dielectric constant = 90.5)[3].

MD simulation. MD simulation is performed in LAMMPS[4] using the all-atom optimized potentials for liquid simulations (OPLS-AA) force-field with the Li^+, PF_6^- and NO_3^- description from previous publication[5]. The LigParGen web-based service[6] is used to obtain the OPLS force-field parameters and partial atomic charges for the

PVDF-HFP, EC, DEC, EMC, DMC and SN cations, which are placed together with the Li^+, PF_6^- and NO_3^- in a simulation box with a dimension of 50 × 50 × 100 nm^3 using PACKMOL[7]. The SN cations are sandwiched by the PVDF-HFP and electrolyte at the beginning of the simulation. Periodic boundary conditions are implemented in all three dimensions. The cutoff of distance for long-range interactions is set to be 12 Å and calculated via the particle-particle-particle-mesh solver. An initial energy minimization at 0 K (energy and force tolerances of 10^{-4} and 10^{-6}) is performed to obtain the ground-state configuration. After this, the system is heated from 0 K to 298 K at constant pressure (1 bar) over 0.2 ns using a Nose-Hoover thermostat, with a timestep of 1 fs and a damping parameter of 100 fs. The system is equilibrated in the constant temperature (298 K), and constant pressure (1 bar) (NpT ensemble) for 2 ns before finally being subjected to 4 ns of constant volume, constant temperature dynamics. The MD simulation of the pure PVDF-HFP separator and electrolyte is performed in the same way as the process described above, but with the removal of SN cations and NO_3^-. Snapshots of the configuration and radial distribution functions are obtained using the Visual Molecular Dynamics (VMD) software[8].

Figures

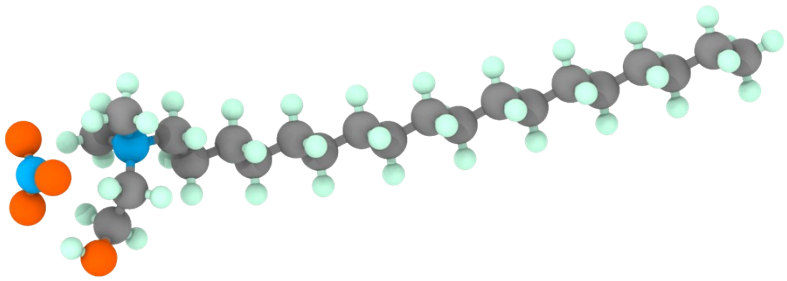

Figure S1. The molecular structure of antistatic agent SN (octadecyl dimethyl hydroxyethyl quaternary ammonium nitrate). C, N, O and H are shown in gray, blue, red and cyan, respectively.

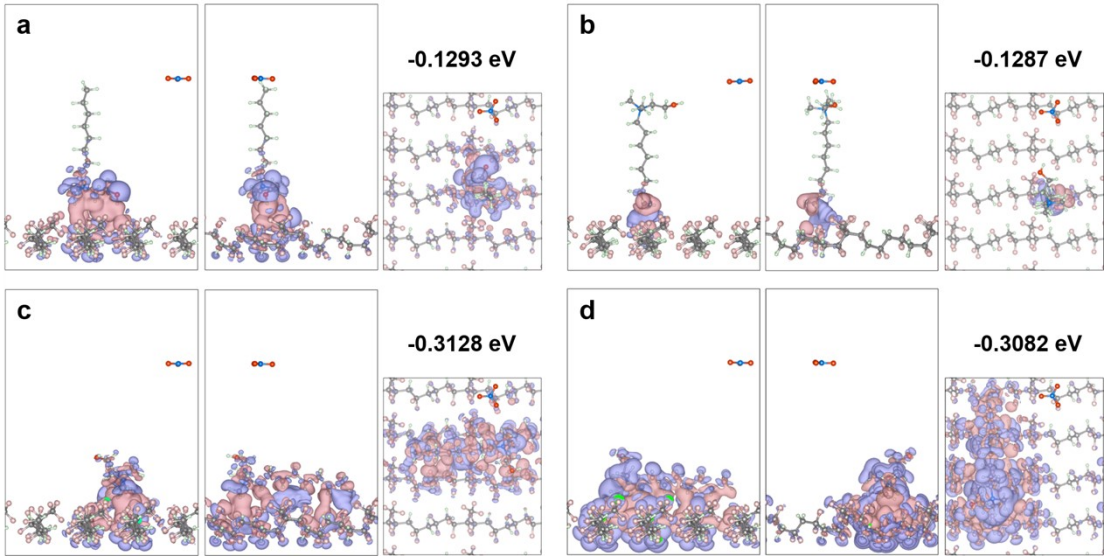

Figure S2. Charge density difference plots of different configurations and absorbing energy of different configurations. (a) SN molecule's head facing down to the PVDF-HFP surface. **(b)** SN molecule's tail facing down to the PVDF-HFP surface. **(c)** SN molecule parallel to the PVDF-HFP chain. **(d)** SN molecule vertical to the PVDF-HFP chain.

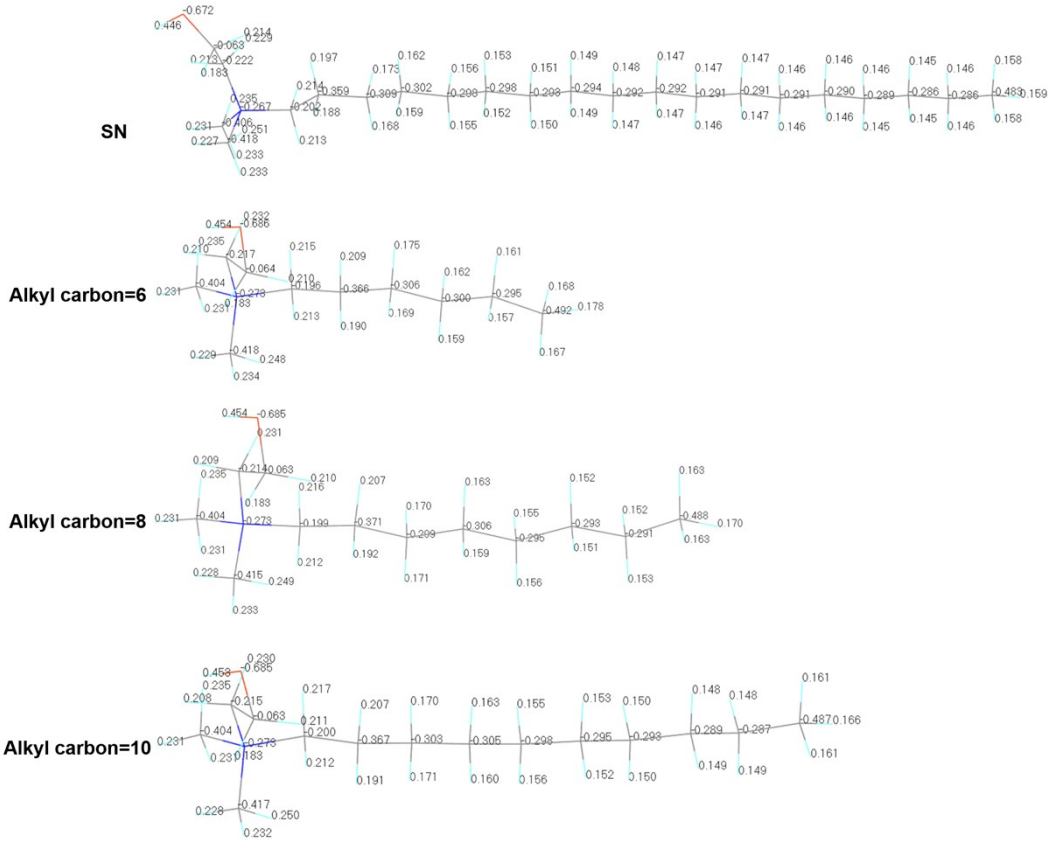

Figure S3. Mulliken charge populations of SN molecules and short versions of SN molecules.

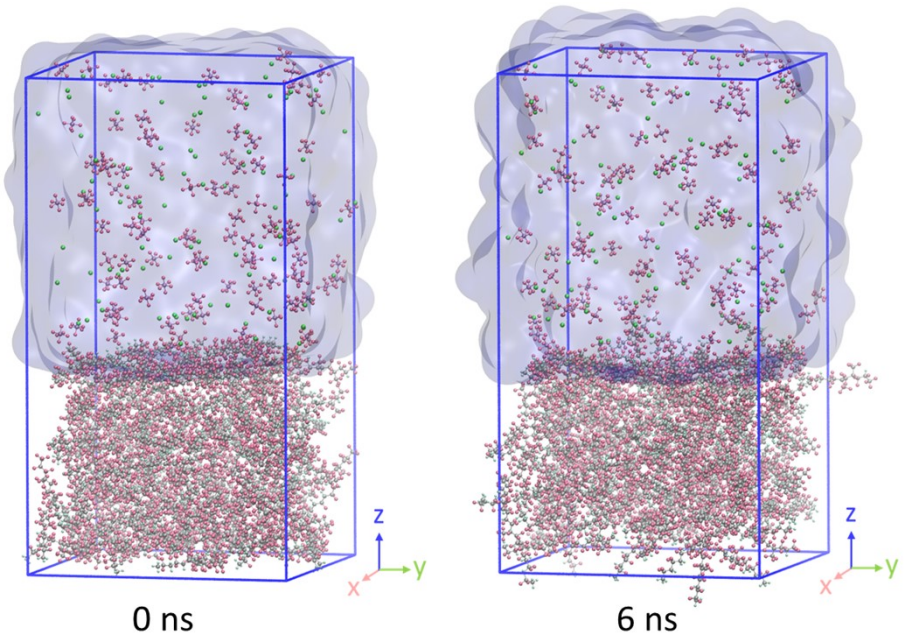

Figure S4. Molecular dynamics (MD) simulation snapshots of the interface between the electrolyte and PVDF-HFP separator at 0 ns and 6 ns.

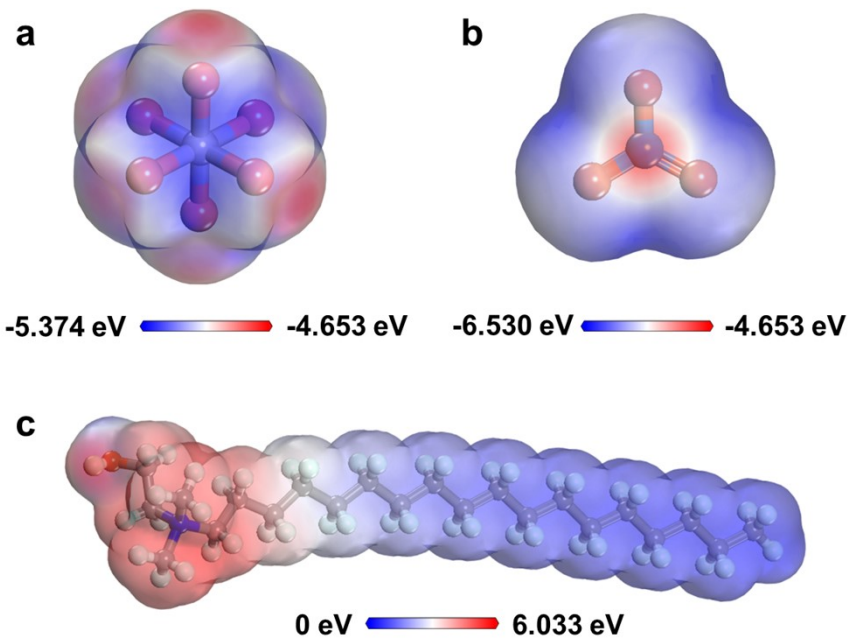

Figure S5. Electrostatic potential of the **(a)** PF_6^-, **(b)** NO_3^-, and **(c)** SN cation.

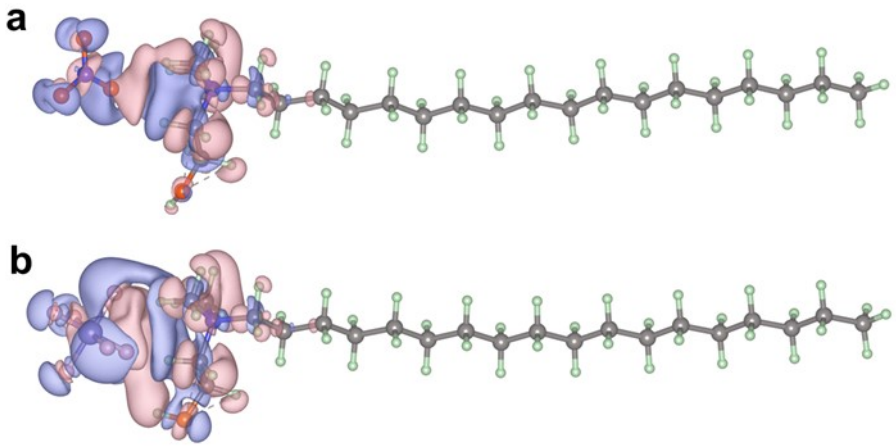

Figure S6. Charge density difference between **(a)** SN-NO_3 and **(b)** SN-PF_6.

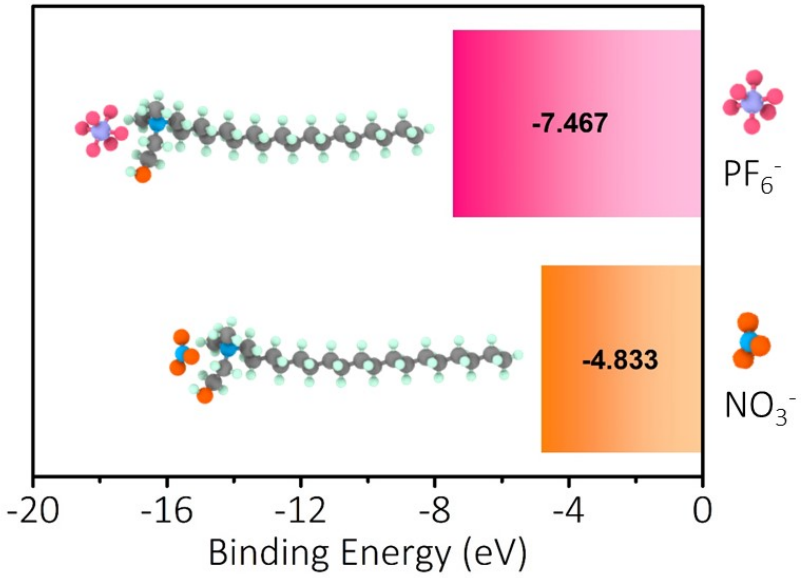

Figure S7. Binding energy of SN-PF_6^- and SN-NO_3^- calculated by density functional theory.

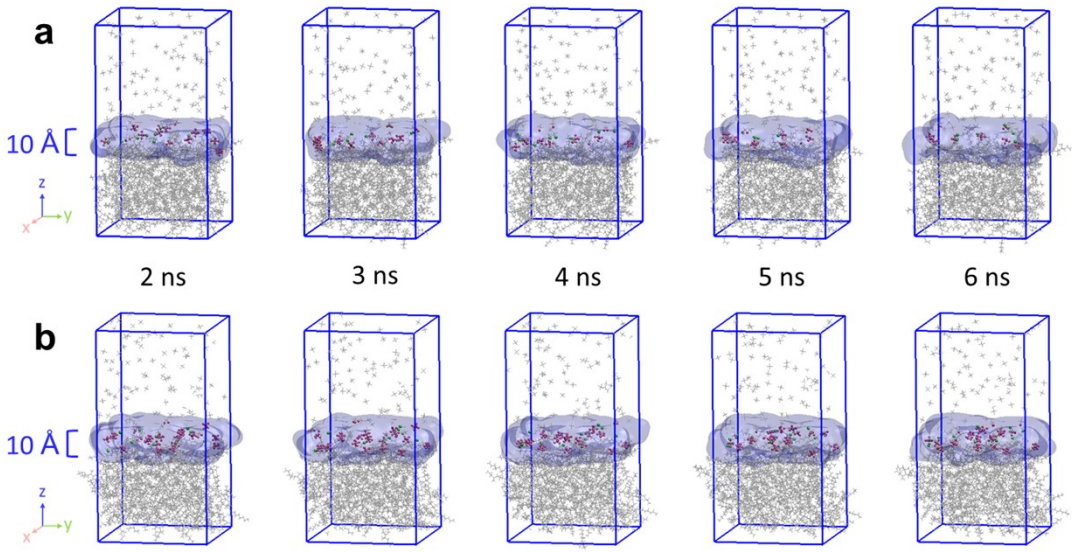

Figure S8. Evolution of the Li salts ion above the **(a)** PVDF-HFP and **(b)** PVDF-HFP/SN separator within a thickness of 10 Å.

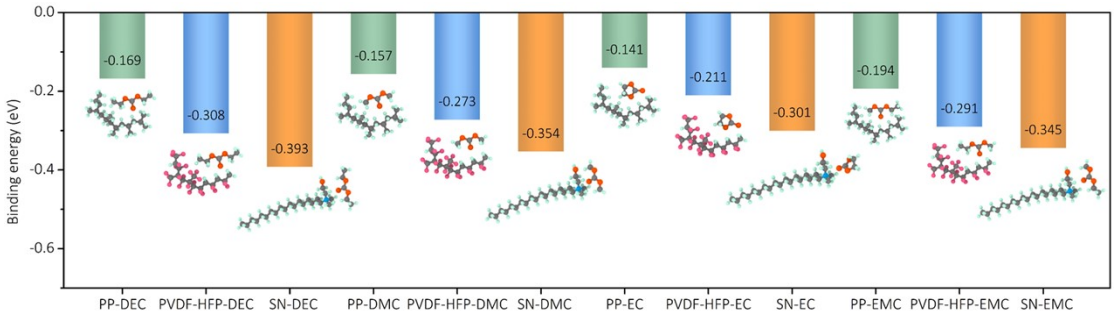

Figure S9. Binding energy of separator molecules and electrolyte solvent molecules.

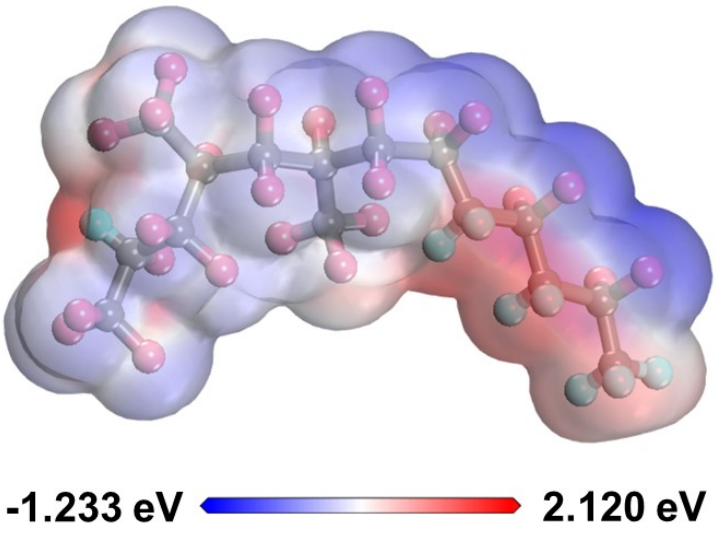

Figure S10. Electrostatic potential of the $(VDF)_3$-$(HFP)_3$ molecule.

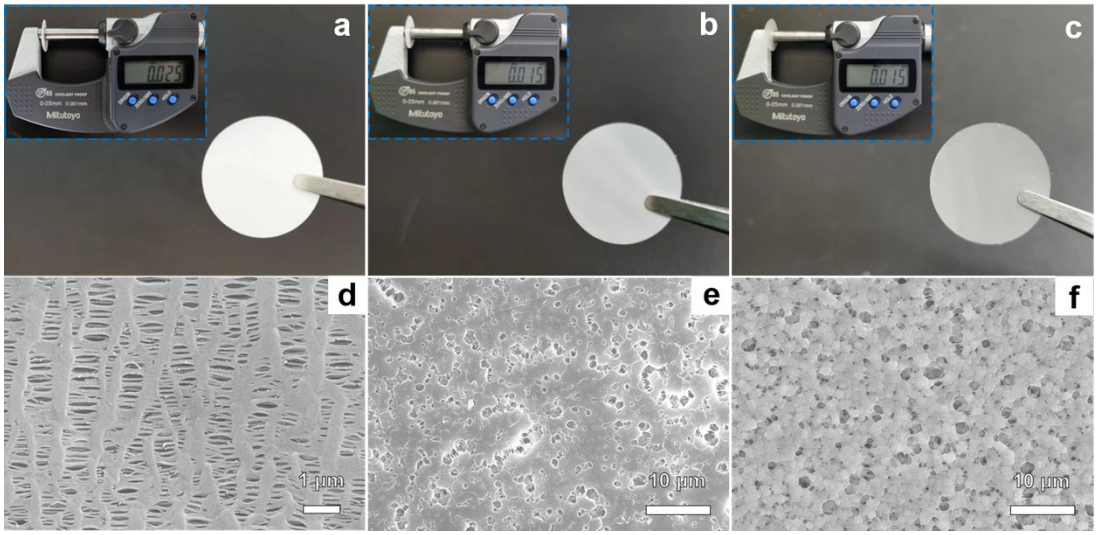

Figure S11. Digital images and thicknesses of different separators. (a) PP separator. **(b)** PVDF-HFP separator. **(c)** PVDF-HFP/SN separator.

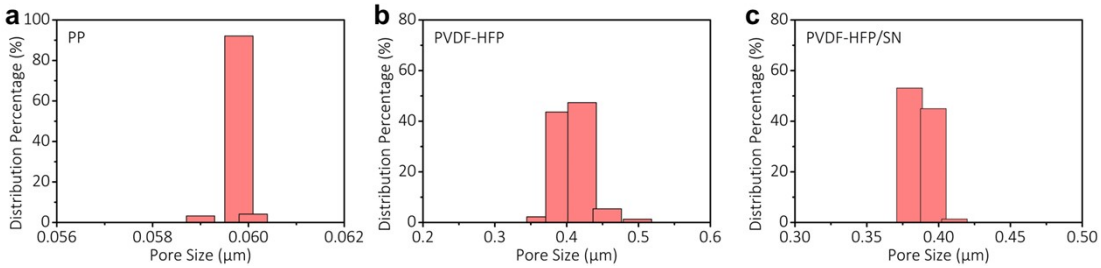

Figure S12. Pore size distribution of different separators. (a) PP separator. **(b)** PVDF-HFP separator. **(c)** PVDF-HFP/SN separator.

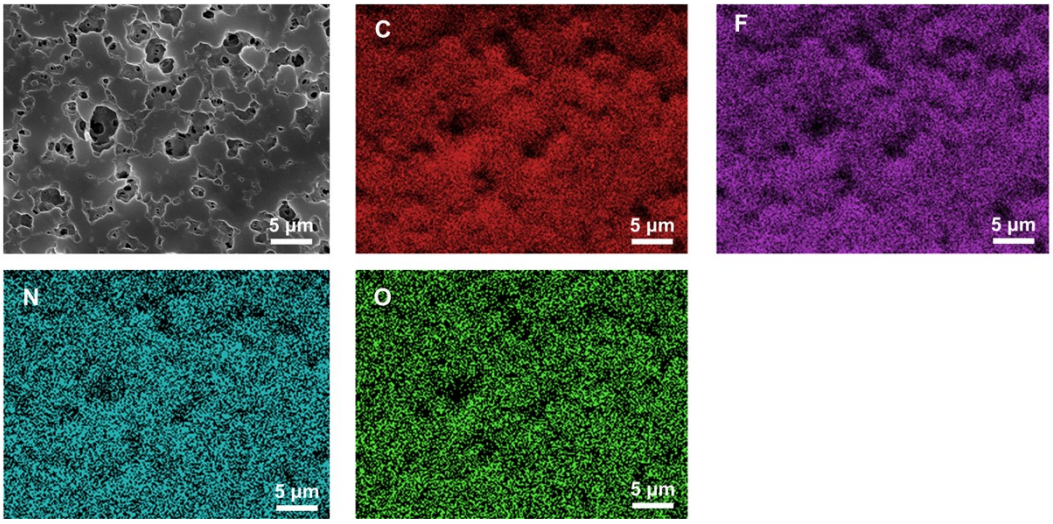

Figure S13. Element mapping images of the PVDF-HFP/SN separator from the top view.

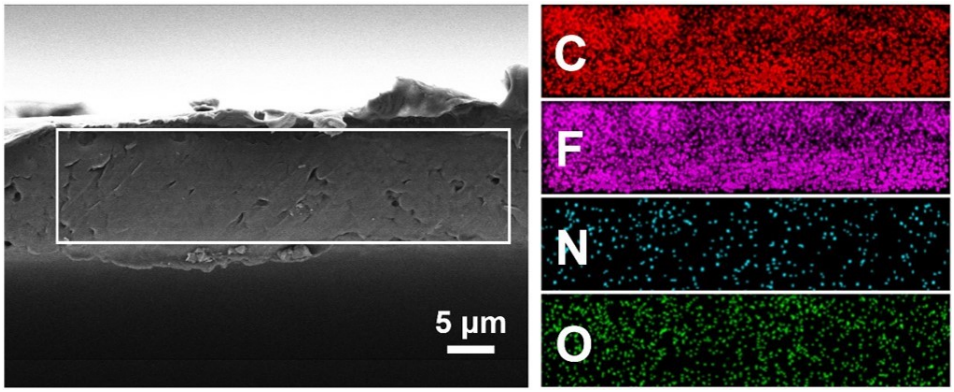

Figure S14. Element mapping images of the PVDF-HFP/SN separator from cross-sectional view.

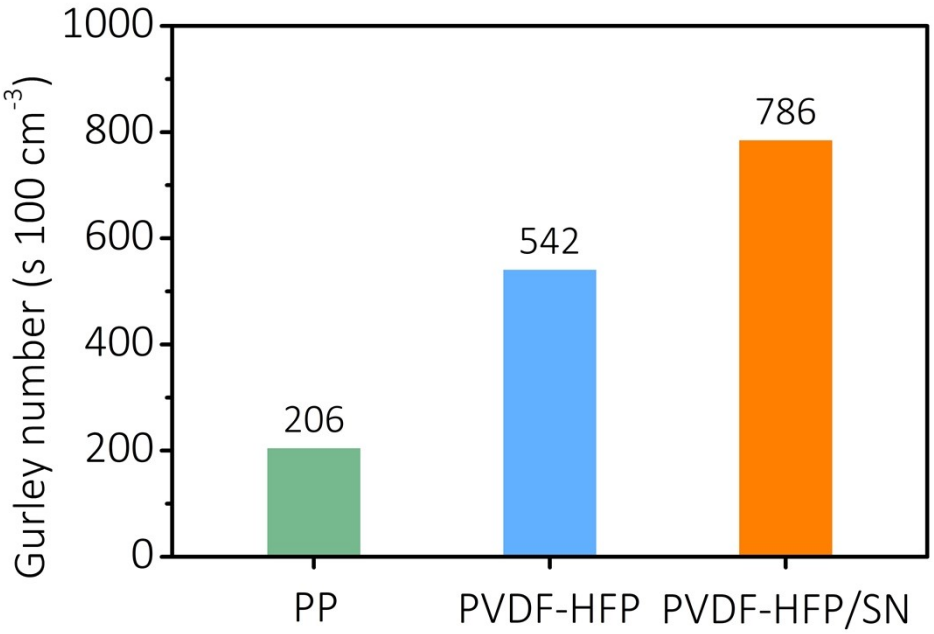

Figure S15. Gurley number of PP, PVDF-HFP and PVDF-HFP/SN separators.

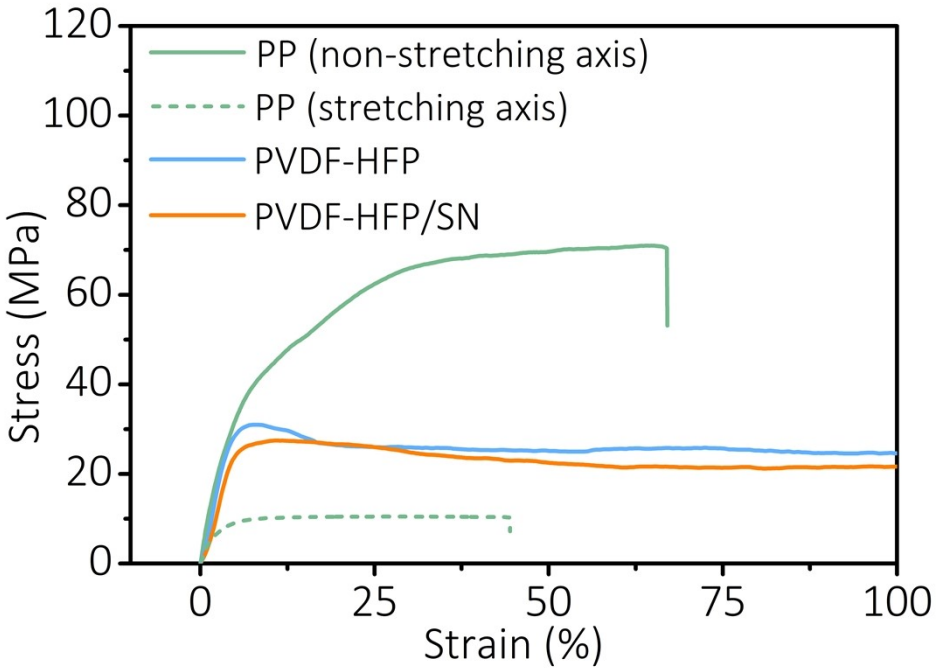

Figure S16. Strain-stress curves of PP, PVDF-HFP and PVDF-HFP/SN separators.

Figure S17. Contact angles of PP, PVDF-HFP and PVDF-HFP/SN separators.

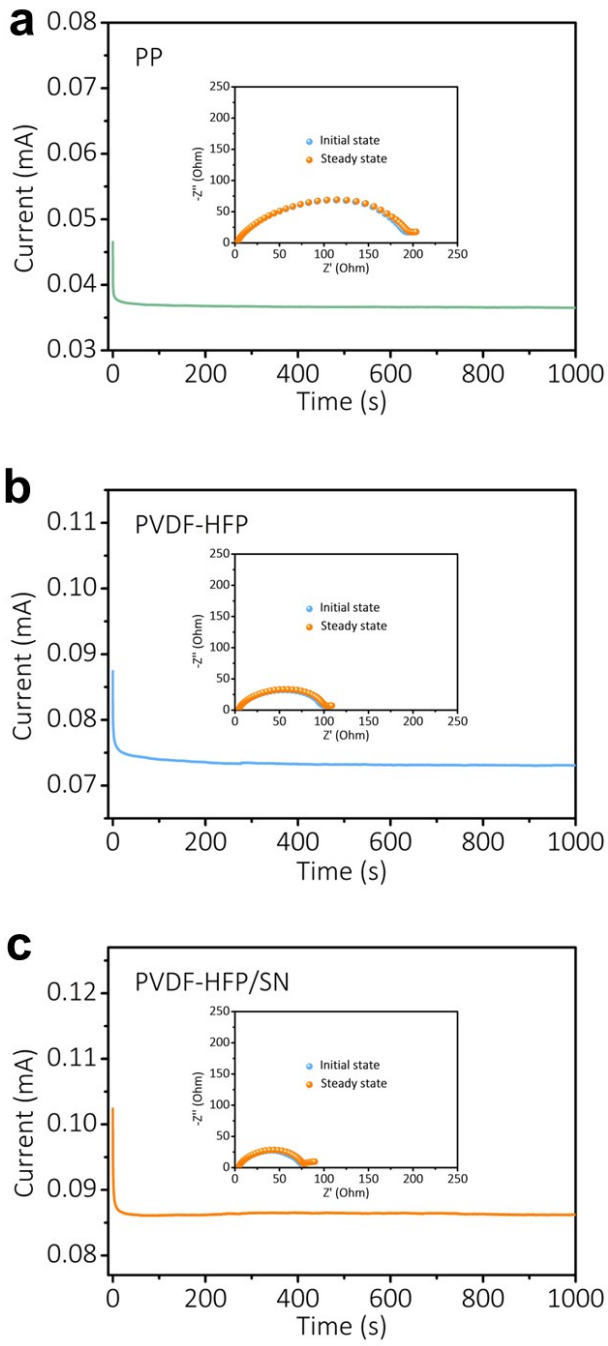

Figure S18. EIS and CA curves of Li||Li symmetric cells. (a) PP separator. **(b)** PVDF-HFP separator. **(c)** PVDF-HFP/SN separator.

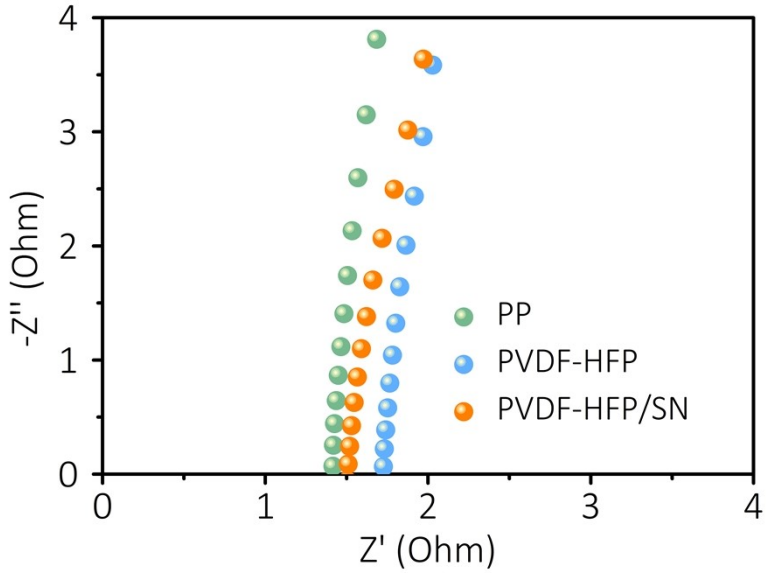

Figure S19. EIS data of SS||SS cells with PP, PVDF-HFP and PVDF-HFP/SN separators.

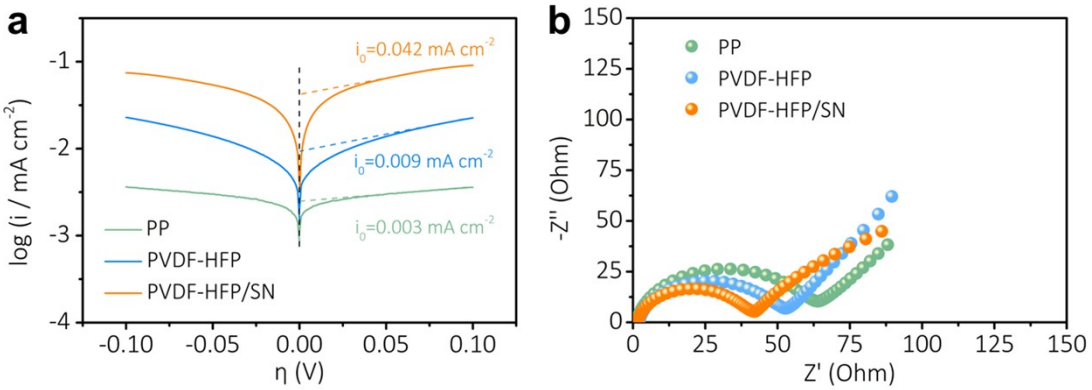

Figure S20. (a) Tafel plots and **(b)** Nyquist plots of LFP||LFP symmetric cell using different separators.

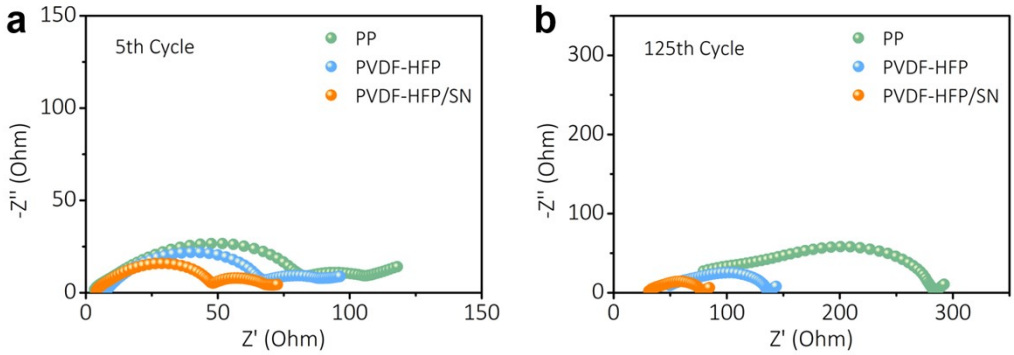

Figure S21. Nyquist plots of Li||Li symmetric cells with different separators at 0.5 mA cm^{-2} with the area capacity of 1 mAh cm^{-2} at different cycles. **(a)** After the 5^{th} cycle, **(b)** after the 125^{th} cycle.

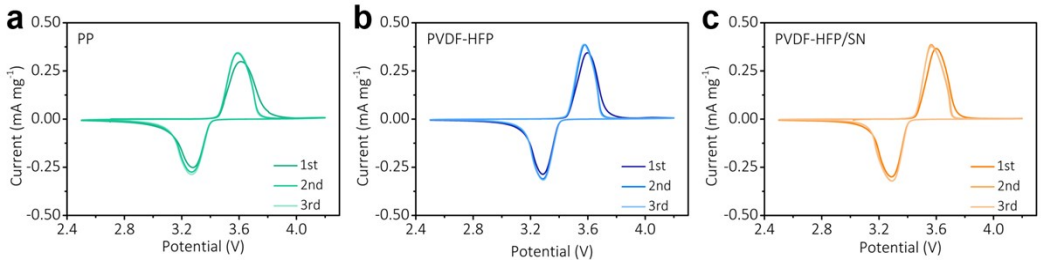

Figure S22. CV curves for the first three cycles of Li||LFP cells. (a) PP separator. **(b)** PVDF-HFP separator. **(c)** PVDF-HFP/SN separator.

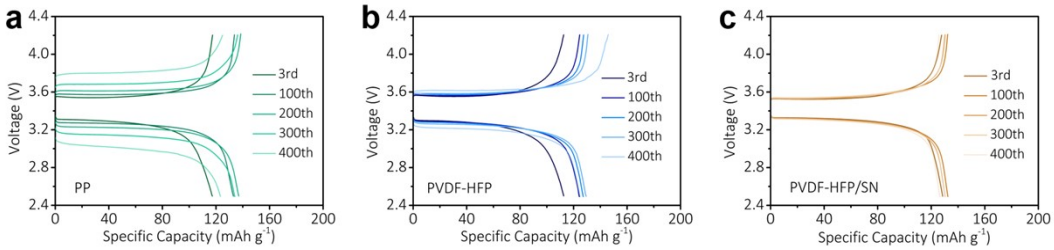

Figure S23. Charge/discharge profiles of different cycles at 2 C using Li||LFP cells. **(a)** PP separator. **(b)** PVDF-HFP separator. **(c)** PVDF-HFP/SN separator.

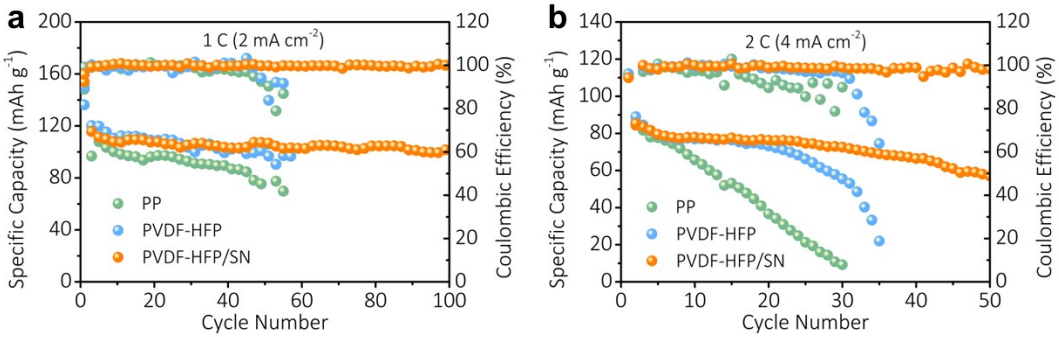

Figure S24. Cycling performances of Li||LFP cells with a high cathode loading of 12 mg cm^{-2} at 1 C and 2 C.

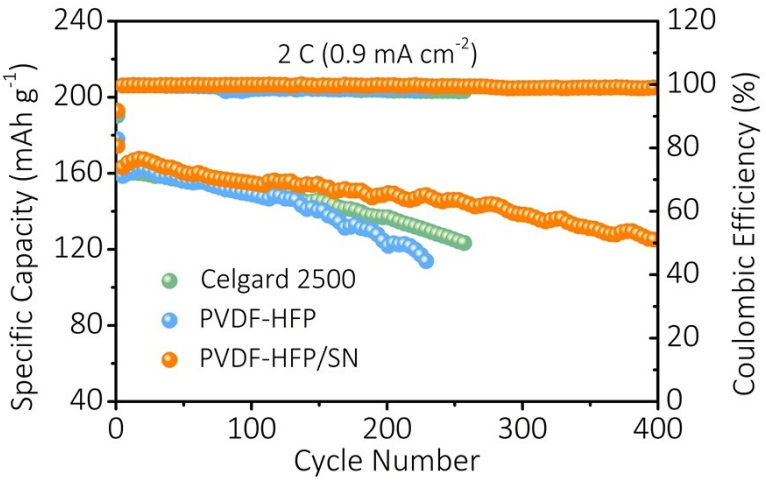

Figure S25. Cycling performances of Li||$LiNi_{0.8}Co_{0.1}Mn_{0.1}O_2$ cells with PP, PVDF-HFP and PVDF-HFP/SN separators at 2 C.

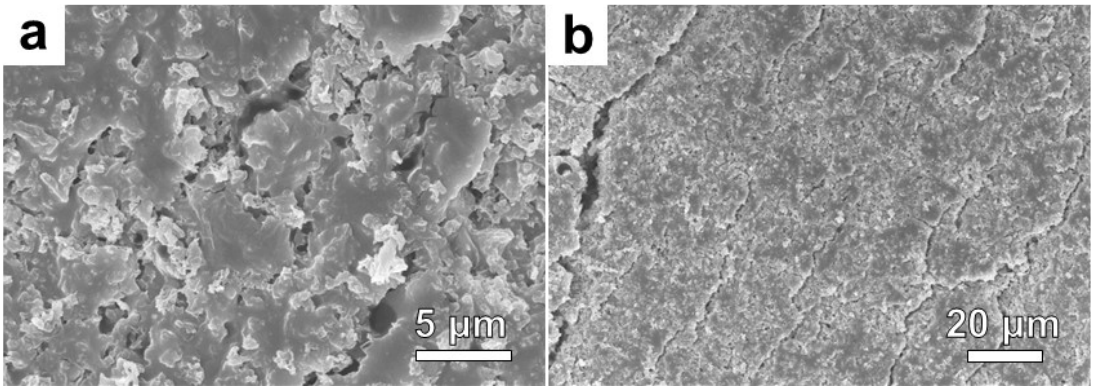

Figure S26. SEM images of Li metal anode disassembled from Li||PVDF-HFP/SN||LFP cell with a high-loading LFP cathode of 12 mg cm^{-2} after 100 cycles at 0.5 C.

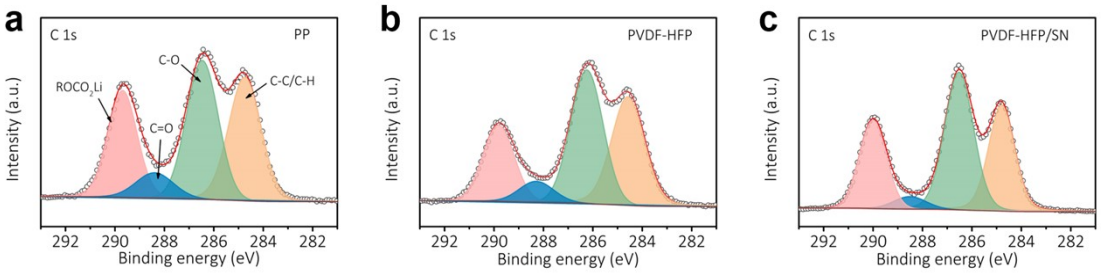

Figure S27. XPS spectra of C 1s on the SEI layer cycled with different separators. **(a)** PP separator. **(b)** PVDF-HFP separator. **(c)** PVDF-HFP/SN separator.

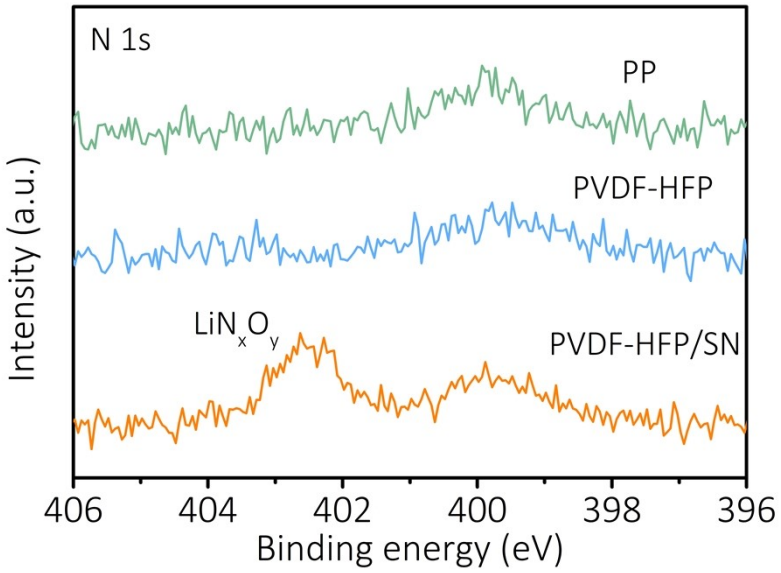

Figure S28. XPS spectra of N 1s on the SEI layer cycled with different separators.

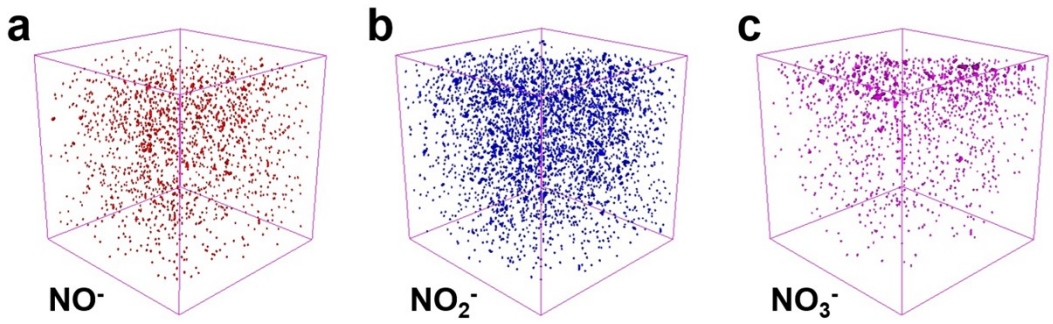

Figure S29. Three-dimensional ToF-SIMS depth spectra of N-containing fragments on the anode cycled with PVDF-HFP/SN separator.

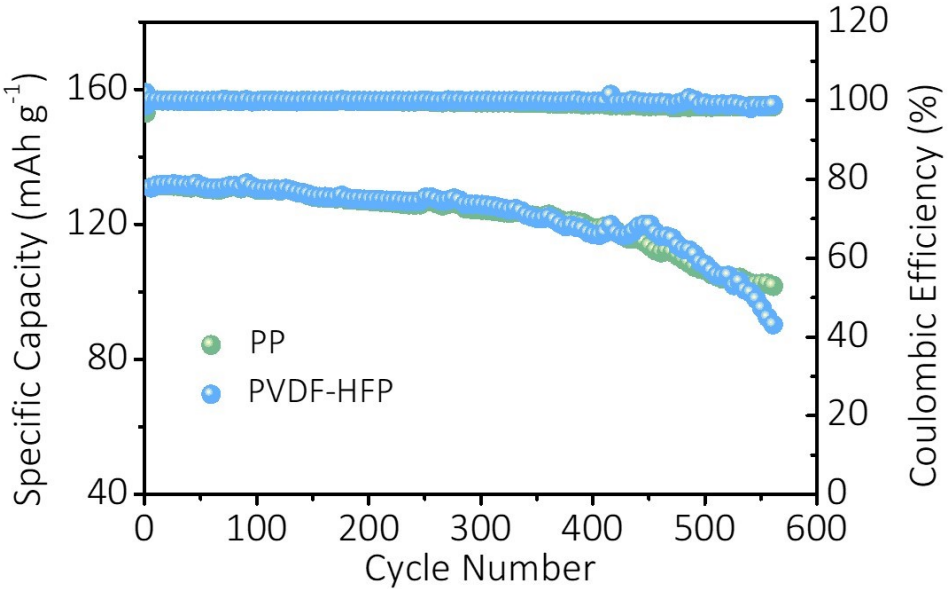

Figure S30. Cycle performances of Li||LFP cells with PP and PVDF-HFP separators at 2 C using the electrolyte that immerses the PVDF-HFP/SN separator for one week.

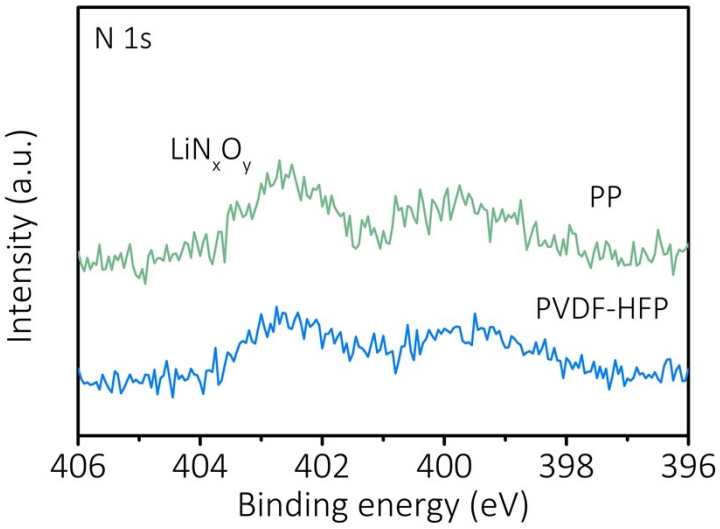

Figure S31. XPS spectra of N 1s in the Li metal anodes cycled with PP and PVDF-HFP separators using the modified electrolyte after 200 cycles at 2 C.

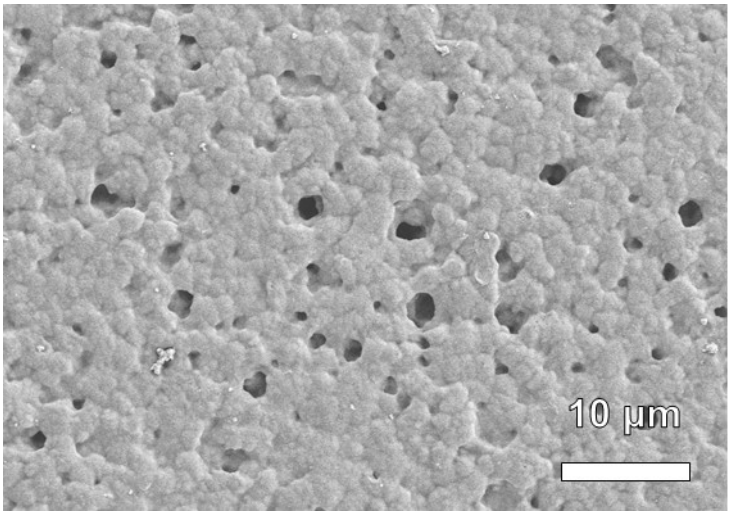

Figure S32. SEM image of the post-cycled PVDF-HFP/SN separator on Li metal side.

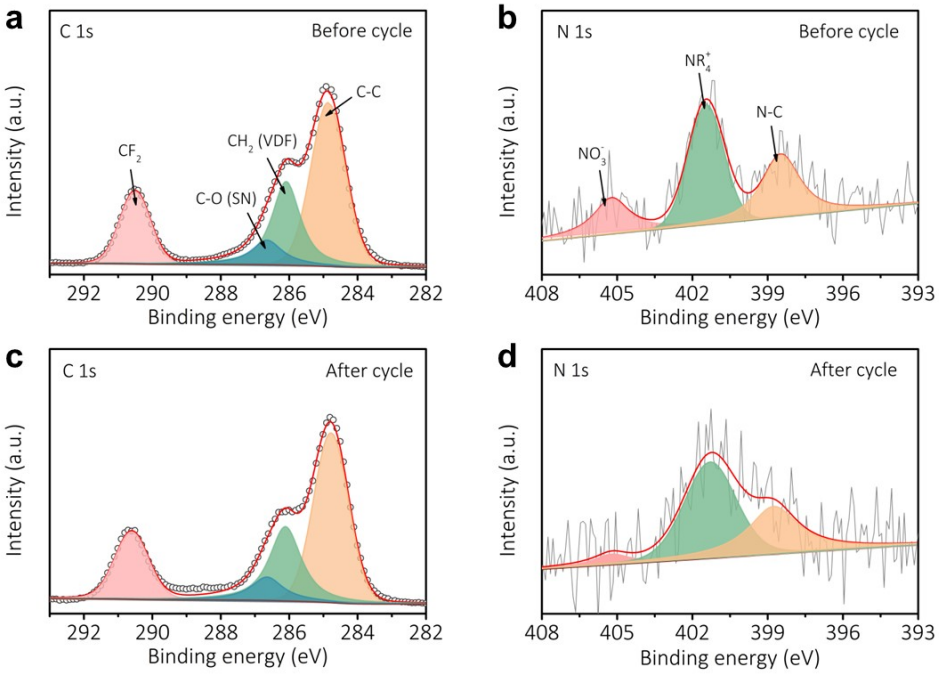

Figure S33. XPS spectra of C 1s and N 1s of post-cycled PVDF-HFP/SN separator on the Li metal side. (a) C 1s and **(b)** N 1s spectra of fresh PVDF-HFP/SN separator. **(c)** C 1s and **(d)** N 1s spectra of PVDF-HFP/SN separator after 200 cycles at 2 C.

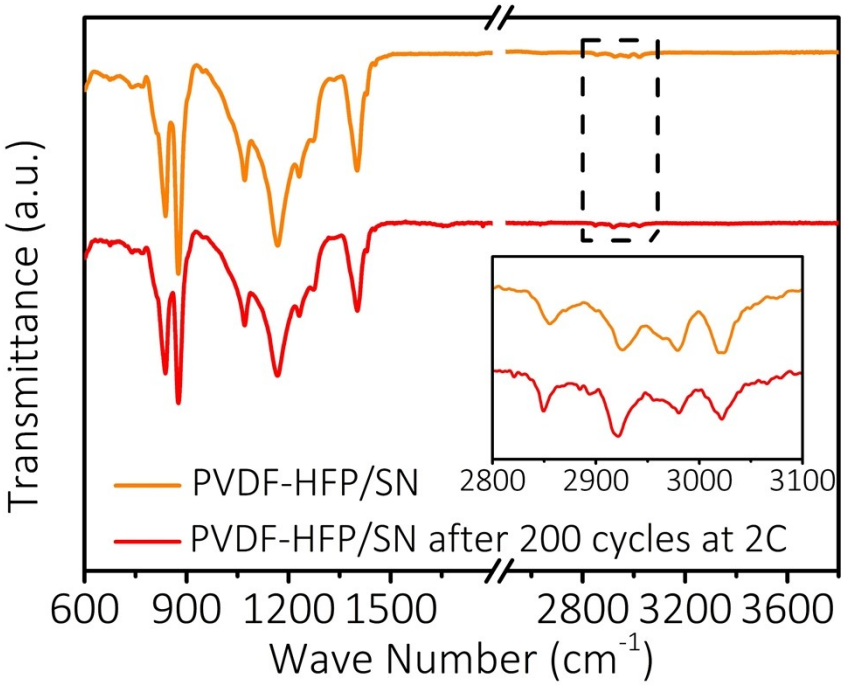

Figure S34. FT-IR spectra of the PVDF-HFP/SN separator before/after 200 cycles at 2 C.

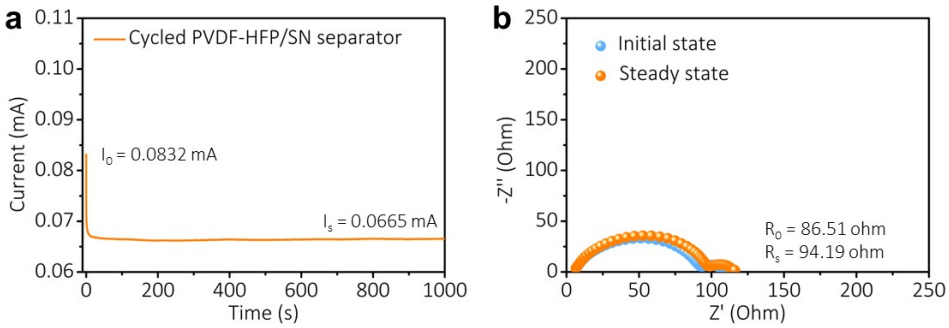

Figure S35. (a) CA curve and **(b)** EIS of Li||Li symmetric cell using post-cycled PVDF-HFP/SN separator.

Table S1 Comparison of the cyclability between the LFP batteries with the PVDF-HFP/SN separator and LFP batteries with other reported separators.

Separator	Cathode loading (mg cm^{-2})	Temperature (°C)	Rates	Cycle number	Retention (%)	Ref. No
PVA/CNC-Li	1.68-1.89	Room temperature	0.7 C	200	89.5	9
PP/DMS	2	Room temperature	1 C	1000	85	10
PVDF/F-PI	/	Room temperature	2 C	1000	70.0	11
PP/h-BN	/	Room temperature	1 C	400	75.9	12
PVDF-HFP/Uio-66-NH_2	/	Room temperature	1 C	1000	74	13
PANI/PVA	1	Room temperature	1 C	100	90.7	14
PP/DLC	1.5	Room temperature	5 C	1000	71.3	15
RESM	1.8	Room temperature	5 C	200	79	16
Porous EAA	/	Room temperature	5 C	200	69	17
PP/$MnCO_3$	3.8	Room temperature	0.5 C	850	90.7	18
PVDF-HFP/SN	2.8	Room temperature	1 C	800	96.9	This work
PVDF-HFP/SN	2.8	Room temperature	2 C	1000	93.4	This work

Table S2. Concentrations of Li^+ and NO_3^- in bare electrolyte and modified electrolyte.

Samples	Concentration of Li^+ ($mg\ L^{-1}$)	Concentration of NO_3^- ($mg\ L^{-1}$)
Bare electrolyte	18.252	0.2718
Modified electrolyte	19.0762	2.1758

Reference

1. Jang, M.; Jung, D.; Lee, J.; Lee, S. M.; Lee, A.; Yim, S.; Song, W.; Myung, S.; Lee, S. S.; Kang, Y. C.; Kwak, S. K.; An, K.-S., PVDF-stimulated surface engineering in ZnO for highly sensitive and water-stable hydrazine sensors. *Appl. Surf. Sci.* **2022,** *585*, 152747.
2. Maurya, A. K.; Mias, E.; Schoeller, J.; Collings, I. E.; Rossi, R. M.; Dommann, A.; Neels, A., Understanding multiscale structure–property correlations in PVDF-HFP electrospun fiber membranes by SAXS and WAXS. *Nanoscale Adv.* **2022,** *4* (2), 491-501.
3. Gunceler, D.; Letchworth-Weaver, K.; Sundararaman, R.; Schwarz, K. A.; Arias, T. A., The importance of nonlinear fluid response in joint density-functional theory studies of battery systems. *Modell. Simul. Mater. Sci. Eng.* **2013,** *21* (7), 074005.
4. Thompson, A. P.; Aktulga, H. M.; Berger, R.; Bolintineanu, D. S.; Brown, W. M.; Crozier, P. S.; in 't Veld, P. J.; Kohlmeyer, A.; Moore, S. G.; Nguyen, T. D.; Shan, R.; Stevens, M. J.; Tranchida, J.; Trott, C.; Plimpton, S. J., LAMMPS - a flexible simulation tool for particle-based materials modeling at the atomic, meso, and continuum scales. *Comput. Phys. Commun.* **2022,** *271*, 108171.
5. Canongia Lopes, J. N.; Pádua, A. A. H., CL&P: A generic and systematic force field for ionic liquids modeling. *Theor. Chem. Acc.* **2012,** *131* (3), 1129.
6. Dodda, L. S.; Cabeza de Vaca, I.; Tirado-Rives, J.; Jorgensen, W. L., LigParGen web server: an automatic OPLS-AA parameter generator for organic ligands. *Nucleic Acids Res.* **2017,** *45* (W1), W331-W336.
7. Martinez, L.; Andrade, R.; Birgin, E. G.; Martinez, J. M., PACKMOL: a package for building initial configurations for molecular dynamics simulations. *J. Comput. Chem.* **2009,** *30* (13), 2157-64.
8. Humphrey, W., Dalke, A. and Schulten, K., VMD: Visual molecular dynamics. *J. Molec. Graphics* **1996,** *14*, 33-38.
9. Mittal, N.; Ojanguren, A.; Cavasin, N.; Lizundia, E.; Niederberger, M., Transient rechargeable battery with a high lithium transport number cellulosic separator. *Adv. Funct. Mater.* **2021,** *31* (33), 2101827.
10. Ren, W.; Zhu, K.; Zhang, W.; Liang, H.; Xu, L.; Wang, L.; Yang, C.; Yang, Y.; Zhang, P.; Wang, F.; Wang, Y.; Li, W., Dendrite-free lithium metal battery enabled by dendritic mesoporous silica coated separator. *Adv. Funct. Mater.* **2023**, 2301586.
11. Qian, Y.; Chen, K.; Feng, Z.; Ouyang, Y.; Lan, Q.; Zhang, C.; Feng, W.; Miao, Y.-E.; Liu, T., A fluorinated-polyimide-based composite nanofibrous separator with homogenized pore size. *Small Struct.* **2023**, 2200383.
12. Liu, X.; Tang, F.; Hu, H.; Huang, H.; Ji, X.; Chen, L.; Liu, Z., Regulation of Li^+ diffusion via an engineered separator to realize a homogeneous lithium microstructure in advanced Li-metal batteries. *ACS Appl. Mater. Interfaces* **2023,** *15* (10), 13761-13771.
13. Guo, M.; Dong, S.; Xiong, J.; Jin, X.; Wan, P.; Lu, S.; Zhang, Y.; Xu, J.; Fan, H., Flexible core-shell PAN/CNTs@PVDF-HFP/Uio-66-NH2 hybrid nanofibers

membrane for advanced lithium-ion batteries separator. *Mater. Today Chem.* **2023,** *30*.
14. Xu, L.; Daphne Ma, X. Y.; Wang, W.; Liu, J.; Wang, Z.; Lu, X., Polymeric one-side conductive Janus separator with preferably oriented pores for enhancing lithium metal battery safety. *J. Mater. Chem. A* **2021,** *9* (6), 3409-3417.
15. Li, Z.; Peng, M.; Zhou, X.; Shin, K.; Tunmee, S.; Zhang, X.; Xie, C.; Saitoh, H.; Zheng, Y.; Zhou, Z.; Tang, Y., In situ chemical lithiation transforms diamond-like carbon into an ultrastrong ion conductor for dendrite-free lithium-metal anodes. *Adv. Mater.* **2021,** *33* (37), e2100793.
16. Ma, L.; Chen, R.; Hu, Y.; Zhang, W.; Zhu, G.; Zhao, P.; Chen, T.; Wang, C.; Yan, W.; Wang, Y.; Wang, L.; Tie, Z.; Liu, J.; Jin, Z., Nanoporous and lyophilic battery separator from regenerated eggshell membrane with effective suppression of dendritic lithium growth. *Energy Storage Mater.* **2018,** *14*, 258-266.
17. Chen, Y.; Mickel, P.; Pei, H.; Wen, Y.; Guan, X.; Wang, Y.; Wang, X.; Mhtachem, O. A.; Zhang, C.; Nie, H.; Zhou, X.; Kral, P.; Xie, X., Bioinspired separator with ion-selective nanochannels for lithium metal batteries. *ACS Appl. Mater. Interfaces* **2023,** *15* (14), 18333-18342.
18. Yan, J.; Liu, F.; Hu, Z.; Gao, J.; Zhou, W.; Huo, H.; Zhou, J.; Li, L., Realizing dendrite-free lithium deposition with a composite separator. *Nano Lett.* **2020,** *20* (5), 3798-3807.